Journal of Porous Materials
https://doi.org/10.1007/s10934-026-01934-x

Carbon foam based microporous Pd(0) catalyst: the rapid and efficient reduction of organic pollutants

Zehra Özçifçi[1] · Nuray Yılmaz Baran[2] · Hakkı Türker Akçay[1] · Kaan Karaoğlu[3] · Talat Baran[2]

Received: 11 March 2025 / Accepted: 9 June 2026
© The Author(s) 2026

Abstract
In the present work, we report the synthesis of a low-cost microporous sucrose-based carbon foam (ACF) with a specific surface area of 591.29 m^2/g, which was used as support for the preparation of a palladium-based (ACF-Pd) heterogeneous catalyst. The prepared ACF-Pd heterogeneous catalyst was characterized using BET, Raman, XPS, XRD, TEM, SEM and EDS methods. The catalytic reduction/decolorization capacity of microporous ACF-Pd was investigated for the reduction of various nitroarenes (2-nitroaniline, 4-nitroaniline, 4-nitrophenol and 4-nitro-o-phenylenediamine) and organic dyes (methyl orange, methylene blue and rhodamine B) by UV-Vis spectroscopy in an aqueous medium, with $NaBH_4$ as the reducing agent at room temperature. The advantages of this method include short reaction times, mild reaction conditions, high yields, easy separation and excellent chemical stability of the catalyst due to its reusability. The results of the catalytic tests showed that the reduction/discoloration reactions of both nitro compounds and organic dyes were successfully carried out within 0–100 s, owing to the strong catalytic ability of ACF-Pd. Moreover, the catalytic reduction of 2-nitroaniline was carried out five times in consecutive run without both noticeable decrease in the catalytic and any change in the morphology of the catalyst, confirming that it is a sustainable and robust nano catalyst.

Keywords Nitroaromatics · Organic dyes · Carbon foam · Organic pollutants · Catalytic degradation

1 Introduction

Today, industrial production is showing an increasing trend due to the growing consumption needs. Accordingly, there is a significant increase in the production of synthetic chemicals. Despite all environmental regulations, the organic pollutants released from these processes seriously threaten our ecosystem. Nitroarenes and industrial organic dyes, both of which pose a serious threat to the ecosystem due to their stable chemical structure and biomagnification potential, are compounds that are toxic to living organisms [1]. The nitro group in nitroarenes makes them valuable in chemical syntheses for a wide range of organic compounds, from drugs to dyes, cosmetics to herbicides, and pesticides [2]. Nitroarens are critical in the production of explosives, preservatives, antioxidants, gasoline additives, corrosion inhibitors, and other industrial chemicals [3, 4]. However, leaks during the use, storage and disposal of these compounds to water pose a serious threat to the environment. Their effects on living organisms are not only toxic; they are also a source of concern due to their mutagenic and carcinogenic properties [5]. In this context, nitroaromatics have been listed as a priority pollutant by the United States Environmental Protection Agency emphasizes the seriousness of the environmental and health risks posed by nitroaromatics [6, 7]. Another class of environmental pollutants is organic dyes, which are heavily used in industry. There are more than 10,000 organic dyes used heavily in industries such as textiles, leather, paper, cosmetics and food [8]. According to the research, it is estimated that about 20% of the dyes used worldwide are discharged to the environment during the dyeing process without any additional treatment [9]. The toxic and carcinogenic effects of these dyes and their

✉ Zehra Özçifçi
zehra.ozcifci@erdogan.edu.tr

[1] Department of Chemistry, Faculty of Arts and Sciences, Recep Tayyip Erdoğan University, Rize, Turkey

[2] Department of Chemistry, Faculty of Science and Letters, Aksaray University, Aksaray 68100, Turkey

[3] Department of Chemistry and Chemical Processing Technologies, Vocational School of Technical Sciences, Recep Tayyip Erdoğan University, Rize, Turkey

Published online: 19 June 2026

degradation products on both the ecosystem and the human body have been identified [10].

Catalytic degradation processes have emerged as a promising method for the removal of pollutants. Catalysts used in these processes, which can generally occur through oxidation, reduction, and hydrolysis, enhance the degradation rate by providing alternative reaction pathways. In catalytic reactions, various nanomaterials such as metal oxides (e.g., ZnO, TiO_2, Co_3O_4) [11–16], rare metals (e.g., Pt, Pd, Rh, Ru) [3, 17–21], enzymes like laccase and peroxidase [22–24], and graphitic carbon nitride can be utilized [25]. Rare metals can be deposited onto various support materials, such as alumina, carbon-based materials (e.g. carbon nanotubes (CNT), graphene, carbon foam and activated carbon), and zeolite, to enhance their catalytic activity, as they tend to cluster at the nano scale. Particularly, activated carbons are effective support materials for metal nanoparticles due to their ability to be produced from diverse sources, low cost, inert structure, high surface area and pore volume.

However, in recent years, carbon-based materials such as carbon nanotubes (CNTs) and graphene have become inadequate for industrial-scale applications due to factors such as a lack of mechanical strength, complex production methods, inability to control pore structures, and high cost [26–28]. Therefore, due to their three-dimensional (3D) hierarchical porous structure, high carbon content, low density, high specific surface area, excellent thermal and chemical stability, electrical conductivity, low production cost, and scalability, carbon foams are strong candidates for a paradigm shift in catalysis compared to traditional carbon-based materials [28, 29]. Especially in reactions carried out at high temperatures and in corrosive chemical environments, carbon foams stand out as a next-generation alternative, exhibiting significantly longer-lasting and more stable performance than classical carbon supports and offering far superior and comprehensive advantages under extreme catalytic conditions such as high-temperature oxidation and hydrogenation. More importantly, thanks to the controllable hierarchical porous structure of carbon foam, the synergistic effect of adsorption and catalysis facilitates the homogeneous distribution of catalytically active species on the carrier surface, thereby optimizing reaction kinetics and achieving maximum efficiency. Thanks to these properties, the carbon foams can be used as adsorbents, electrodes, catalytic supports, and electromagnetic barriers [30].

Carbon foam materials are produced by through gas release during the pyrolysis reactions, during chemical reactions with the additives, or due to the decomposition of the chemical called blowing agent directly added to the starting material. Although fossil fuels are commonly used in the production of such materials, carbon foam materials can also be produced from renewable, inexpensive, and accessible sources such as sucrose and tannin, with blowing agents such as boric acid, phenolic resin, sodium bicarbonate, pentane, and metal nitrates [31, 32].

In the literature, carbon foams have demonstrated improved activity and long-term stability not only in conventional catalytic systems but also in applications such as green chemistry, fuel cells, CO_2 reduction, water splitting, and biocatalysis [33–36]. Metal catalysts (e.g., Pd@CF, Fe@CF, Ni@CF) supported on carbon foam have shown superior performance in the catalytic reduction of nitroarenes in aqueous systems, providing high conversion efficiencies and recyclability [34, 35, 37–40]. Additionally, carbon foam-supported catalysts have been successfully employed in the degradation of other organic pollutants, such as phenolic compounds, azodyes, and pharmaceutical residues, via both reductive and oxidative pathways [38, 41–43]. Given these advantages, carbon foam presents a highly promising support material for the development of efficient and reusable catalytic systems aimed at removing organic pollutants from the environment.

In the presented study, an activated carbon material based on high microporous carbon foam, activated with sulfuric acid, was produced and used as a solid support for Pd(0). The catalytic performance of the obtained catalyst on environmental pollutants was investigated using four nitroarene (2-nitroaniline (2-NA), 4-nitroaniline (4-NA), 4-nitrophenol (4-NP), 4-nitro-o-phenylenediamine (4-NPD)) and three organic dyes (methyl orange (MO), methylene blue (MB), rhodamine B (RhB)) selected as model compounds.

2 Experimental

2.1 Materials and characterization methods

All chemicals used in experimental studies were of the reagent grade (Sucrose (99%, Sigma-Aldrich 84100), Zinc (II) nitrate ($Zn(NO_3)_2.6H_2O$, ≥98%, Sigma-Aldrich 228737), Sulfuric acid (H_2SO_4, %95–98, Sigma-Aldrich 258105), and Hydrochloric acid (HCl, 37% Sigma-Aldrich 258148) and purchased from Sigma-Aldrich. Pure water (UP) was used in all experiments.

The surface area and porosity measurement were studied by BET (Brunauer–Emmett–Teller) analyzer (Quantachrome Autosorb IQ2, USA) via nitrogen adsorption–desorption isotherms at 77 K. The degassing of all samples was performed under vacuum at 105 °C for 15 h before each measurement. The surface area, total pore volume, and pore size distribution of CFs were calculated by BET method, the QSDFT (Quenched Solid Density Functional Theory), The HK (Horvath-Kawazoe) method and BJH (Barret-Joyner-Halenda) method [44–46]. The surface

morphology was visualized with Scanning electron microscope (SEM) (JEOL JSM 6610 instrument). X-ray diffraction (XRD) patterns were recorded by using Rigaku smart lab system to analyze the crystal structure of the samples. A Hitachi HT-7700 with a 40–120 eV Lanthanum hexaboride electron beam gun was used to record Transmission electron microscope (TEM) images of samples. Surface functional groups were determined by XPS (Specs-Flex XPS instrument), and graphitization degrees were determined by Raman spectroscopy at 532 nm with the WITech alpha 300R.

2.2 Synthesis of activated carbon foam (ACF)

The activated carbon foam was prepared by following method previously reported [31] with sucrose as the carbon source and zinc(II) nitrate as the blowing agent. 5 g sucrose and 0.5 g $Zn(NO_3)_2$. $4H_2O$ were dissolved in 6 mL of water. The clear solution was heated in oven at 120 °C to obtain viscous liquid, and then temperature was elevated to 230 °C to form the carbon foam. The carbon foam was grounded with a mortar and boiled in 0.1 mol.L^{-1} HCl solution for 15 min to remove soluble materials and zinc compounds. Afterward, the solid material was washed with water until a neutral filtrate was obtained and dried at 80 °C for 24 h. The sample was labeled as CF.

For the activation step, CF was mixed with H_2SO_4 in a 4:1 ratio (H_2SO_4:sample, wt: wt) and heated at 85 °C for 8 h, then kept in an oven at 100 °C overnight. The pasty solid sample was carbonized in a tubular furnace at 800 °C for 1 h at a heating rate of 10 °C.min^{-1} under an inert N_2 atmosphere at a flow rate of 100 mL.min^{-1}. The sample was boiled with 0.1 mol.L^{-1} HCl for 30 min and filtered, then washed with hot distilled water and dried at 100 °C for 24 h and labeled as ACF.

2.3 Synthesis of Pd(0) doped activated carbon foam (ACF-Pd)

The palladium-doped activated carbon was prepared according to literature [21]. Activated carbon foam (1 g) was added to ethanol and ultrasonicated to obtain a suspension. $PdCl_2$ (200 mg) was added to the suspension. The reaction mixture was refluxed for 16 h on magnetic stirrer. At the end of the reaction, the suspension was centrifuged and washed with water and ethanol three times each, and dried in an oven at 70 °C.

2.4 Catalytic degradation studies

Within the scope of the Green Chemistry approach, the catalytic performance of the microbeads at low energy consumption for RhO and MO degradation was tested at the room temperature. Additionally, to minimize the environmental impact, preliminary catalytic tests were conducted in water by varying the catalyst amount from 5 mg to 50 mg.

2.4.1 The catalytic reduction of nitro arens

1 mL of nitroaromatics (1×10^{-4} M) and 0.5 mL of $NaBH_4$ (0.05 M) solution were placed in a quartz cuvette and stirred for 2 min at room temperature. Then, 5 mg of ACF-Pd catalyst was added to this mixture, and the changes in the characteristic absorbance bands of nitroaromatics were followed by UV-Vis spectrophotometer to monitor the progress of the reactions. After the reduction reactions, ACF-Pd catalyst was collected by filtration, washed with water and ethanol, dried and made ready for recovery studies.

2.4.2 The catalytic reduction of organic dyes

1 mL of organic dye solution (1×10^{-5} M), 0.5 mL of $NaBH_4$ (0.05 M), and 5 mg of ACF-Pd catalyst were added to a quartz cuvette and stirred at room temperature. The progress of the catalytic reactions was followed by recording the changes in the characteristic bands at 466 nm for MO, 667 nm for MB, and 556 nm for RhB dye. After the reduction process was completed, the ACF-Pd catalyst was separated from the reaction mixture by a method like the one mentioned above, washed, and dried.

3 Results and discussion

3.1 Characterization of activated carbon foam (ACF)

The carbon foam production consists of two stages. In the first stage, when the sucrose and $Zn(NO_3)_2$ solution is heated to 120 °C, caramelization begins as a result of hydrolysis of sucrose into glucose and fructose. In the second stage, the temperature was increased to 230 °C. As sucrose units continue to hydrolyze, polymeric carbon structures are formed as given in Fig. 1. At 125 °C, NO_x gas is released during decomposition of $Zn(NO_3)_2$. The released NO_x gases swell the carbonized material and form carbon foam. Activated carbon is prepared by chemical activation method of carbon foam material with sulfuric acid at 800 °C in an N_2 atmosphere.

NO_x gas is released during the decomposition of $Zn(NO_3)_2$. The corresponding reaction proceeds according to Eqs. 1, 2.

$$C_{12}H_{22}O_{11(s)} + Zn\,(NO_3)_2.6H_2O_{(s)} \underset{125?,\,\triangle}{\rightarrow} \underset{230?,\,\triangle}{\rightarrow} C_{foam\,(s)} + ZnO_{(s)} + N_{2\,(g)} + NO_{x\,(g)} + H_2O_{(g)} + CO_{2\,(g)} \quad (1)$$



Fig. 1 Carbon foams obtained from sucrose with 10% concentrations of $Zn(NO_3)_2$

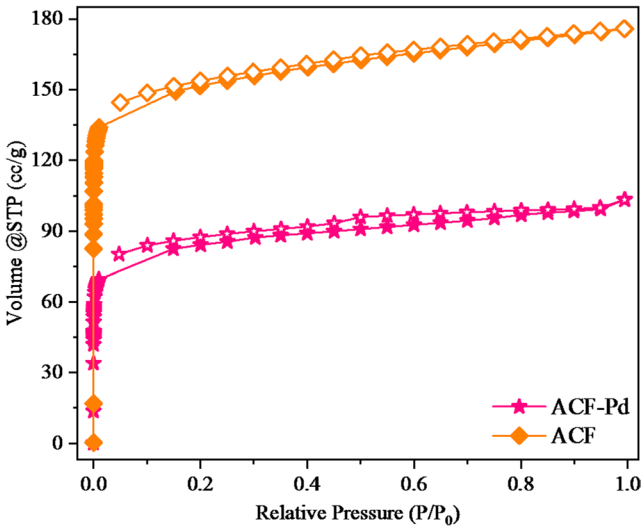


Fig. 2 N_2 adsorption/desorption isotherms of ACF

$$2\,ZnO_{(s)} + C_{foam\,(s)} \rightarrow 2\,Zn_{(g)} + CO_{2\,(g)} \quad (2)$$

$Zn(NO_3)_2.6H_2O$, a strong oxidizer, decomposed and reacted with sucrose to form gases such as N_2, NO_x, and CO_2. The NO_x gases released act as oxidants to burn the sugar, swelling the carbonized material and forming carbon foam. ZnO nanoparticles formed from the decomposition of zinc nitrate not only act as abrasives to further activate the carbon foam and create greater porosity with increasing temperature but also provide a framework to prevent the collapse of the molten porous sugar during carbonization. Thus, carbon foam formation occurs in a single step. Upon completion of the carbonization process, the ZnO was reduced with HCl and then washed with pure water until the pH was neutral and dried [32, 47, 48]. Pd(0)–doped ACF was obtained by boiling ACF in ethanol with $PdCl_2$ under reflux conditions for 16 h and labeled as ACF-Pd. The structures of samples were characterized by BET, XRD, TEM and SEM analysis.

Various activation agents, such as H_2SO_4, H_3PO_4, $ZnCl_2$, and KOH, are used to determine the surface area and pore size of activated carbon. H_2SO_4, one of these, plays a significant role in microporosity in the production and improvement of carbon materials [31, 49]. During the reaction, H_2SO_4 decomposes and SO_x gases are formed, which are removed from the structure with heteroatom oxides. The surface area of sucrose carbonized without activation with a blowing agent was calculated as 247 m^2/g [50]. The removal of Zn species formed during the carbon foam production phase from the sample structure led to the formation of mesoporosity, and the subsequent use of H_2SO_4 as an activating agent created micropores in the final product, resulting in a heterogeneous pore distribution.

The N_2 adsorption and desorption isotherms obtained for both ACF and ACF-Pd samples are shown in Fig. 2. The isotherms consist of sharp adsorption indicating microporosity at the relative pressure (P/P_0) value less than 0.1, and the plateau indicating mesoporosity at the region of high relative pressure. Due to these features, the isotherms can be considered a combination of Type 1 and Type 4 isotherms according to the International Union of Pure and Applied Chemistry (IUPAC) classification [51–53].

The surface characteristics of ACF and ACF-Pd were given in Table 1. The specific surface area, total pore volume, and average pore diameter of ACF were calculated by the BET method as 591 m^2/g, 0.272 cm^3/g and 1.87 nm, respectively [44]. The micropore distribution of ACF were calculated by HK method, and the micropore volume was obtained as 0.231 $cm^3.g^{-1}$ (inset of Fig. 3a) [46, 51–53].The mesoporosity characterized by a plateau in the relative high-pressure region of the isotherm of ACF was investigated by the BJH method.

Table 1 Surface and porosity characteristics of ACF and ACF-Pd

	SSA ($m^2.g^{-1}$)	$V_{total\ pore}$ [a] ($cm^3.g^{-1}$)	V_{micro} [b] ($cm^3.g^{-1}$)	V_{meso} [c] ($cm^3.g^{-1}$)	% V_{micro}	% V_{meso}	Pore Dia. (nm)
ACF	591	0.27	0.23	0.04	85	14	1.87
ACF-Pd	297	0.16	0.13	0.03	80	19	2.15

[a] $V_{total\ pore}$ at $P/P_0 \approx 0.99$,

[b] V_{micro} at 2 nm (HK method)

[c] V_{meso} > 2 nm (BJH method)

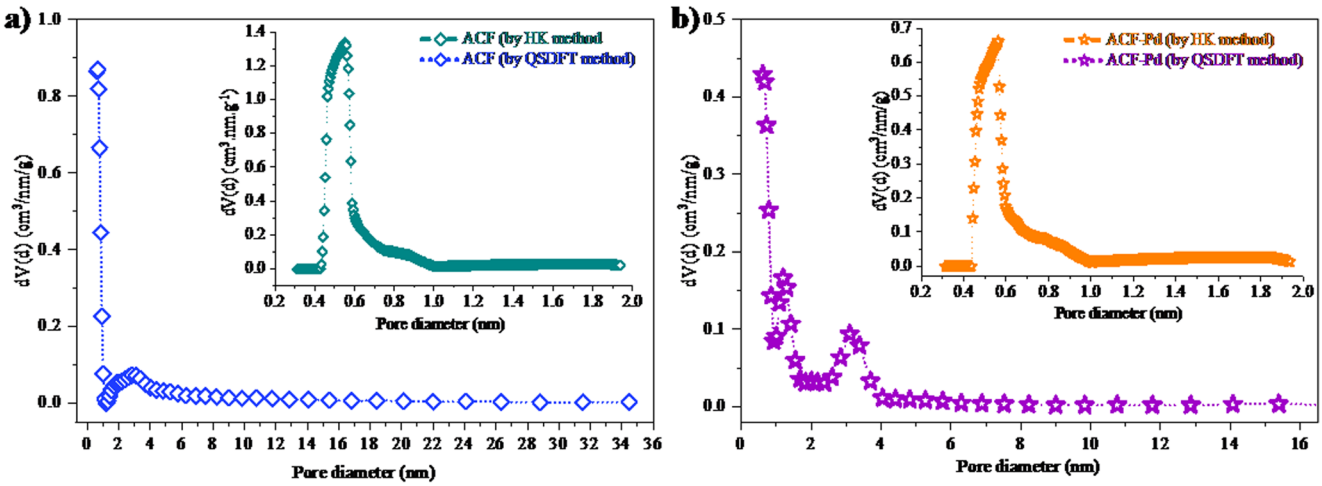


Fig. 3 The pore size distribution of ACF and ACF-Pd

Accordingly, the mesopore volume of ACF was calculated as 0.039 cm^3/g [44].The fact that the micropore volume constitutes 85% of the total pore volume confirms that the material consists mainly of micropores. The pore size distribution of ACF calculated with QSDFT is given in Fig. 3a [45]. The porosity characteristics of ACF-Pd are quite similar to those of ACF except for the decrease in pore volumes and surface areas resulting from Pd doping onto the structure. The H4–type hysteresis observed in the isotherm of ACF–Pd (Fig. 2) suggests a slit pore structure. The specific surface area, total pore volume, micro and mesopore volume and average pore diameter of ACF-Pd were calculated as 296 m^2/g, 0.160 cm^3/g, 0.128 cm^3/g, 0.030 cm^3/g and 2.15 nm, respectively (Table 1). In both samples, the total pore volume obtained by BET were in good agreement with the sum of the micro and mesopore volumes obtained by the methods of QSDFT and HK. The micropore distributions of ACF-Pd are given in Fig. 3b.

Raman spectroscopy is an important technique widely used in the analysis of microstructural properties and graphitization degrees of carbon-based materials. Figure 4 shows 2-peak and 4-peak deconvolution of the Raman spectra of ACF. The G band (1594 cm^{-1}) represents the graphitic structures of sp^2 hybridized carbon atoms, while the D band (1347 cm^{-1}) indicates structural disorders and the presence of non-graphitic carbon atoms [31, 54, 55]. The D_1 (1344 cm^{-1}), G_1 (1594 cm^{-1}), D_2 (1237 cm^{-1}) and G_2 (1536 cm^{-1}) bands indicate the heterogeneous structural properties of the material and the effect of functional groups. The ratios I_D/I_G = 1.13, I_{D1}/I_{G1} = 1.48, and I_{D2}/I_{G2} = 0.26 indicate that the ACF sample contains a higher degree of structural disorder and an increase in the number of functional groups on the surface (Table 2). Specifically, the ratio $I_{D1}/I_{G1}>1$, indicates increased structural disorder and a more amorphous or edge-dense sample, while lower ratios indicate a more crystalline, graphitic structure [31,

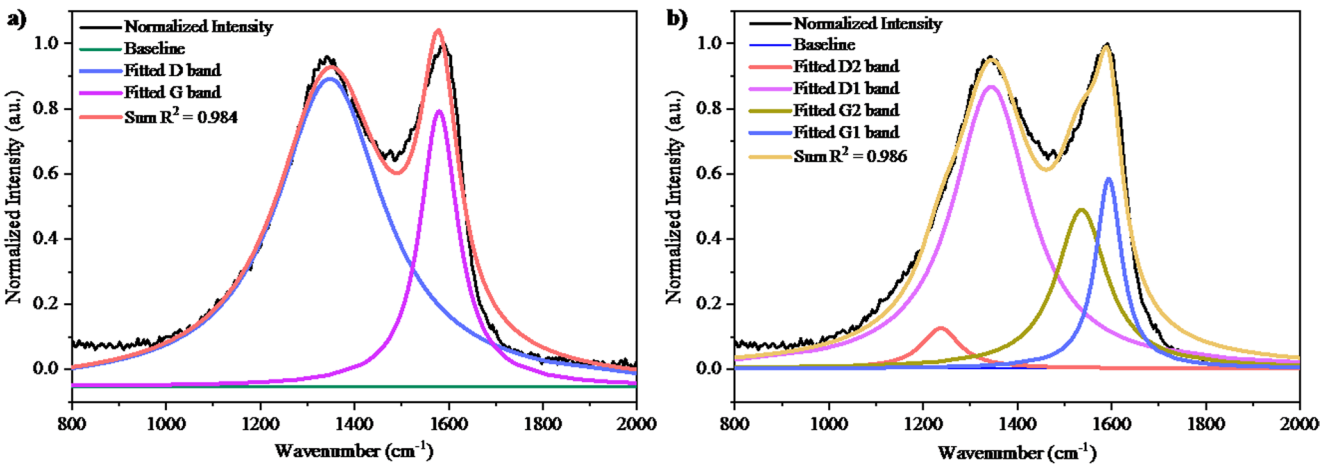


Fig. 4 Deconvolution of Raman spectra into (**a**) 2 peaks, (**b**) 4 four peaks of ACF

Table 2 Deconvolution results of Raman spectrum

Sample	G_1		G_2		D_1		D_2		I_{D1}/I_{G1}	I_{D2}/I_{G2}	R^2*	G		D		I_D/I_G	R^2*
	ν	FWHM	ν	FWHM	ν	FWHM	ν	FWHM				ν	FWHM	ν	FWHM		
ACF	1594	67.5	1536.16	130.45	1344.23	197.03	1236.86	99.10	1.48	0.26	0.99	1579.48	97.87	1347.66	277.34	1.13	0.98

32]. The ratio $I_{D2}/I_{G2}<1$ indicates the presence of heteroatom-doped oxygen functional groups on the ACF surface. These functional groups indicate that ACF has high surface energy combined with structural disorder, and that metal catalysts such as Pd(0) can readily be loaded onto this structure. Thus, Pd(0) nanoparticles adhere strongly to the disordered regions, preventing agglomeration and maximizing catalytic activity [56]. Therefore, ACF-supported Pd(0) catalysts are expected to exhibit high performance in various environmental and chemical reactions.

XPS spectroscopy analysis was performed to examine the surface chemical composition and functional groups of ACF (Fig. 5). The examination of the overall ACF spectrum determined that the structure consisted of components containing only carbon (C) and oxygen (O), with the zinc (Zn) and sulfur (S) elements being removed from structure (Fig. 5a). The peak observed around ~1225 eV is due to high-binding energy Auger signals in the case of carbon materials [57]. High-resolution spectra of the C1s and O1s regions were deconvolved using the Gaussian function (Fig. 5). When the C1s spectrum is examined in Fig. 5b, the main peak with a bond energy of ~284.2 eV is attributed to C–C/C–H bonds, indicating the presence of graphitic (sp^2) or aliphatic carbon (sp^3) structures. The peak observed around ~285.1 eV corresponds to C–O bonds that may originate from phenol or alcohol groups. The peak observed at ~286.3 eV is attributed to C-O-C epoxide functional groups and the peak at ~288.0 eV is attributed to C=O (carbonyl, quinones, and ketones) groups. The broad peak around ~289.4 eV is attributed to COOH carboxyl groups found in carboxylic acid or ester structures. The O1s spectrum (Fig. 5c) shows the various oxygen functional groups present on the ACF surface. The peak at ~529.8 eV represents C=O in quinones, carboxyl, and carbonyl groups. The peak at ~531.4 eV represents oxygen atoms double-bonded to carbonyl groups (C=O) oxygen atoms in anhydrides and oxygen atoms (-OH) in hydroxyl groups, while the peak at ~532.5 eV is attributed to single-bonded oxygens in the C–O–C or C–OH groups. The peak at ~533.0 eV represents oxygen atoms in carboxyl groups (–COOH or COOR). Furthermore, the peak at ~535.2 eV indicates chemisorbed water or the presence of surface hydroxyls. XPS results revealed that ACF is abundant in oxygen-containing surface functional groups, including hydroxyl (–OH), carbonyl (C=O), and carboxyl (–COOH), which play a significant role in increasing surface polarity and enhancing the adsorption affinity of polar molecules [31, 32, 58–60]. Furthermore, these functional groups allow adsorbates to adhere more strongly to the surface through hydrogen bonding and electrostatic interactions. Due to the weak acidic nature of the carboxyl and hydroxyl groups, ACF can also exhibit high performance in the adsorption of basic species. Furthermore, these surface groups form structures that can serve as active centers in catalytic applications and facilitate

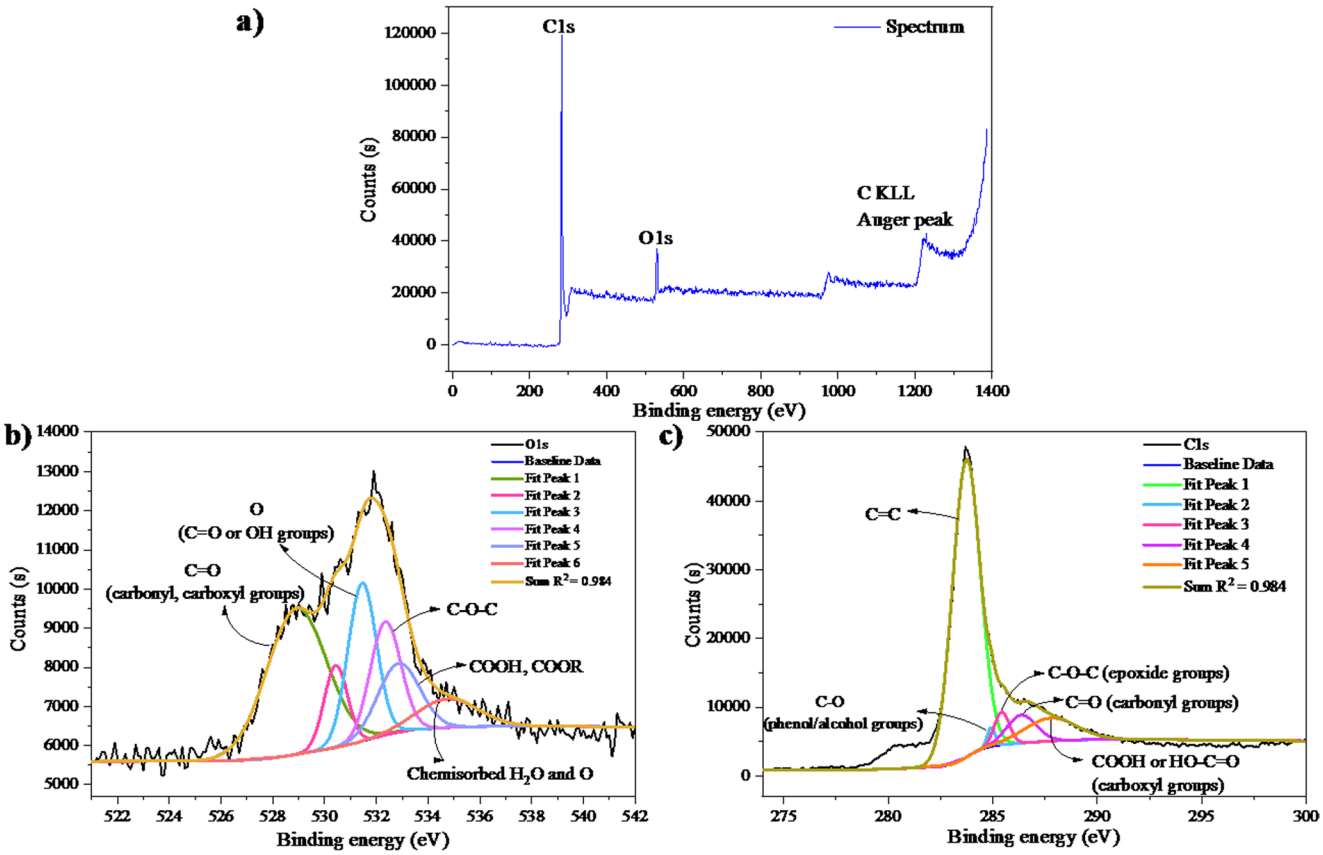


Fig. 5 Deconvolution of ACF; (**a**) general spectrum (**b**) C1s spectra, (**c**) O1s spectra

the binding of metal ions to the surface, enabling ACF to be used as a catalyst support. Therefore, the increase in surface functional groups significantly increases both the adsorption capacity and catalytic potential of ACF.

In the XRD pattern of ACF (Fig. 6) the broad diffraction band observed at about 2θ = 22.8º can be assigned to the amorphous carbon structures, and the weak and broad band observed at about 2θ = 43.7º can be attributed to the graphitic structure [61]. The XRD pattern of ACF-Pd is given in Fig. 6. The band observed at about 2θ = 22.40° was caused by amorphous carbon structure. The sharp diffraction peaks at 2θ = 40.18°, 46.54°, 68.15°, 82.13° and 86.62° were observed, which can be indexed to (111), (200), (220), (311) and (222) planes of face-centered cubic (fcc) lattice belonged to Pd (JCPDS = 46–1043) [62]. In the Debye-Scherer method, it can mainly be used to evaluate the peak expansion, and crystallite size caused by dislocation [63].

SEM and TEM images of ACF-Pd (Figs. 7 and 8) confirm the structure of the material. The microporous structure of the material is limited to the data obtained by surface area measurements due to the resolution limit of SEM. On the other hand, Pd(0) deposition on ACF were

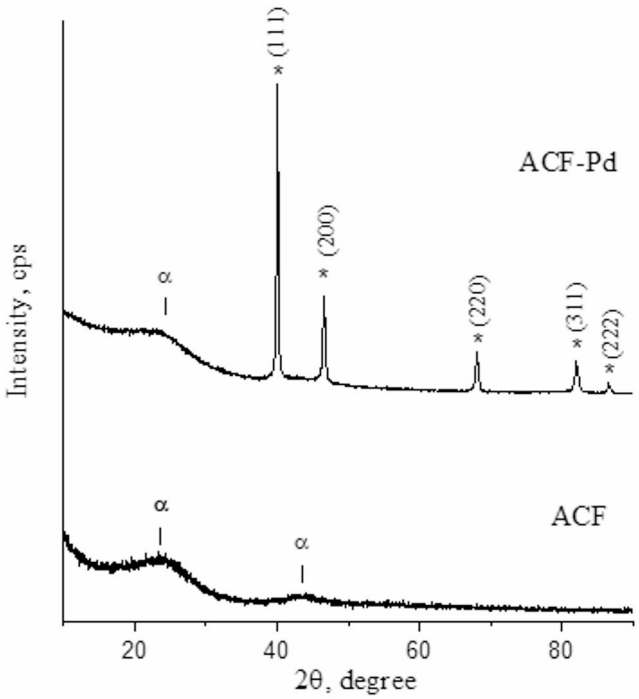


Fig. 6 XRD pattern of ACF-Pd (*: Pd(0), α: carbon)

observed in SEM images of ACF-Pd. The EDS spectrum of the material, together with XRD, confirms the presence of Pd(0) in the structure of ACF-Pd. The presence of sulfur observed in the EDS spectrum of the material is due to the sulfuric acid used during activation. In the TEM images of ACF-Pd, Pd(0) clusters were observed as darker dots. As seen in Fig. 7, Pd(0)s generally show a homogeneous distribution.

3.2 Catalytic behavior of ACF-Pd towards reduction of organic pollutants

The catalytic activity of ACF-Pd catalyst was investigated in the catalytic reduction of environmental pollutants, such as some nitro aromatics (2-NA, 4-NP, 4-NA and 4-NPD) (Fig. 9) and organic dyes (MO, MB and RhB). Catalytic reductions were carried out in the presence of a reducing agent, $NaBH_4$. The reduction reactions were followed spectrochemically by UV-Vis spectroscopy, monitoring the decrease in the characteristic absorbance peaks of both nitroaromatics and organic dyes during the reaction times.

As seen in Fig. 9a, the aqueous solution of 2-NA exhibits two strong characteristic absorbance bands at 412 nm and 281 nm. After the addition of 5 mg ACF-Pd catalyst to the reaction mixture containing 2-NA+$NaBH_4$, it was observed that the absorbance band of 2-NA at 412 nm decreased with time and completely disappeared after 25 s. Additionally, it is observed that the absorbance band at 281 nm was shifted to 292 nm. During this process, it was determined that the yellow solution of 2-NA became colorless due to catalytic reduction. These findings confirm that the ACF-Pd catalyst successfully converted 2-NA to o-phenylenediamine. To evaluate catalytic performance of ACF-Pd, the catalytic reduction of 2-NA was also carried out without the ACF-Pd catalyst, and it was found that the reaction did not proceed to completion for a long time. This finding confirmed that ACF-Pd catalyst played an indispensable role in the catalytic reduction of 2-NA. Then, the catalytic ability of

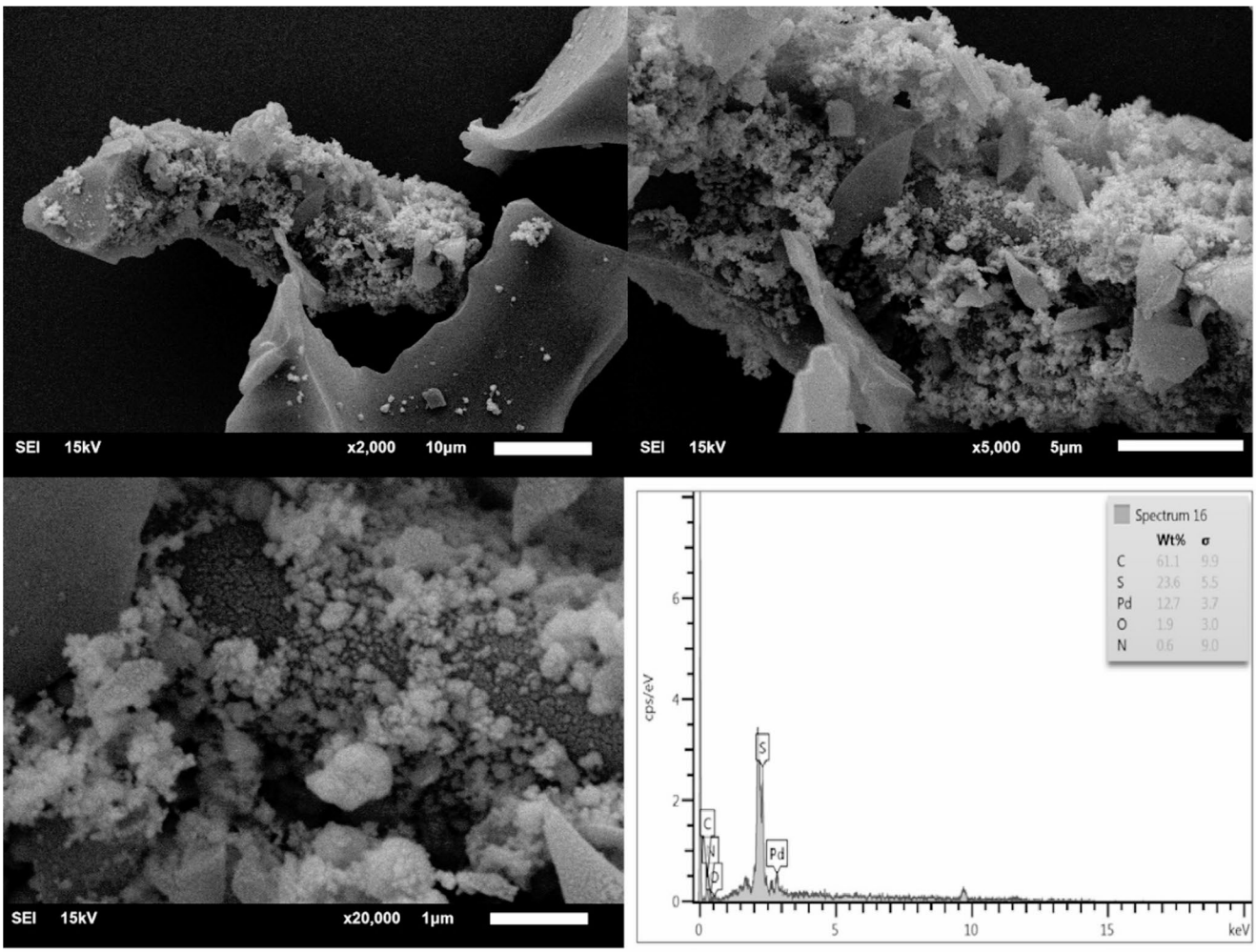


Fig. 7 SEM images of ACF-Pd

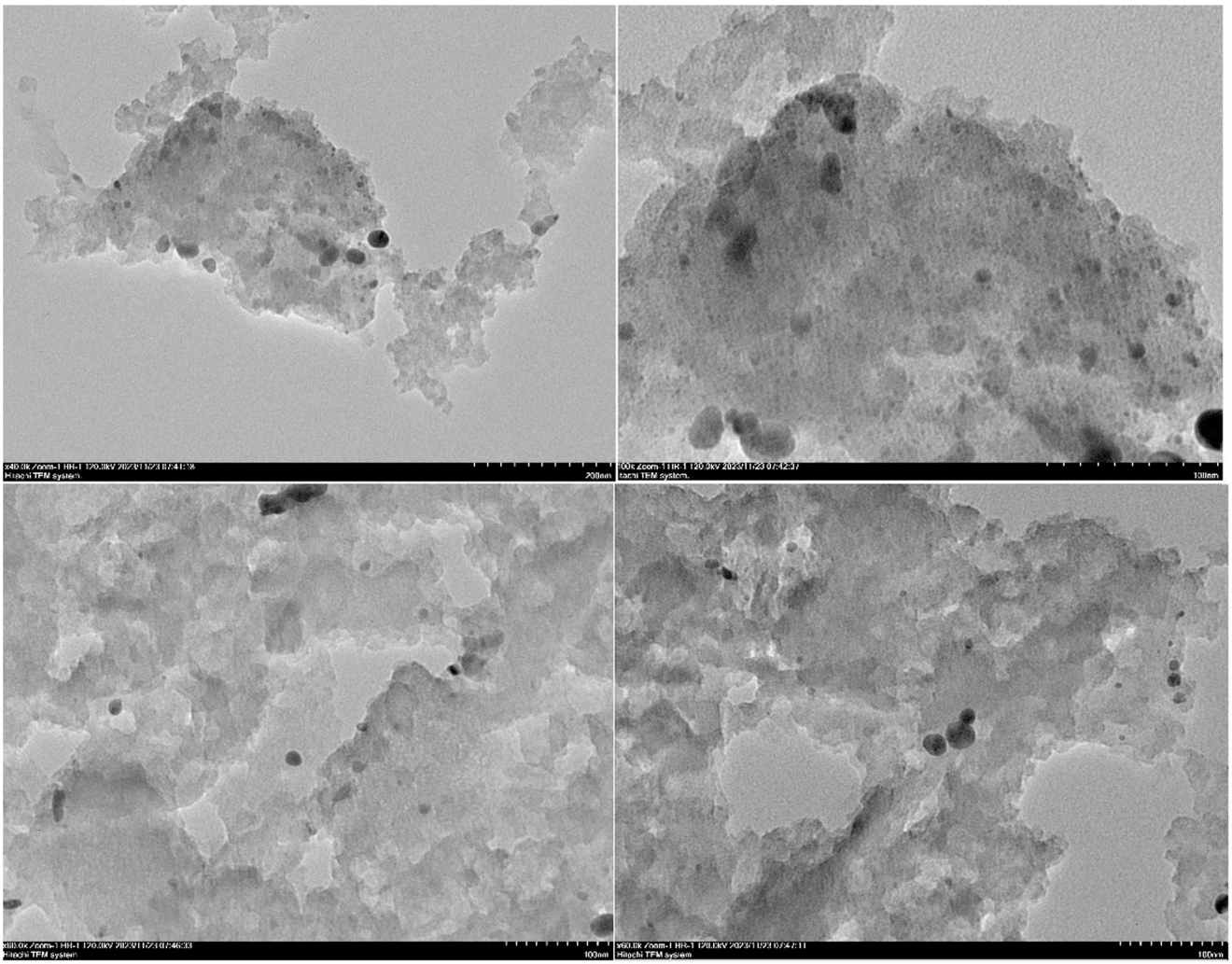


Fig. 8 TEM image of ACF-Pd

ACF-Pd catalyst was also tested in the reduction of nitro aromatics such as 4-NP, 4-NA and 4-NPD. In Fig. 9b, it is shown that the aqueous solution of 4-NP exhibited a strong absorbance band at wavelength of 318 nm. It was observed that with the addition of $NaBH_4$ to the aqueous solution of 4-NP, the solution color turned bright yellow, and the band at 318 nm of 4-NP shifted to 404 nm. These findings indicate that the 4-nitrophenolate ion was formed and confirm that the reaction occurs via this intermediate product. After adding 5 mg ACF-Pd catalyst to the reaction medium, the peak intensity at 404 nm started to decrease and completely disappeared within 50 s. In addition, a new peak appeared at 302 nm indicating the formation of 4-aminophenol. It was also observed that the bright yellow color of 4-nitrophenolate ion became colorless by the end of the reaction. As seen in Fig. 9c and d, the aqueous solution of 4-NA exhibited a strong absorbance band at 384 nm, while the aqueous solution of 4-NPD exhibited two absorbance bands at 268 nm and 405 nm. Catalytic reduction of the 4-NA and 4-NPD by $NaBH_4$ over ACF-Pd were studied by monitoring UV/vis. absorption spectral changes over time. As the reactions proceeded, the intensities of the peaks at 384 nm for 4-NA and at 405 nm for 4-NPD started to decrease with time and these peaks completely disappeared in 45 s for 4-NA and in 100 s for 4-NPD. Simultaneously with these changes, a new peak was observed at 308 nm in the spectrum of 4-NA, while the peak at 268 nm shifted to 307 nm in UV/vis. spectra of 4-NPD. At the end of the reduction processes, it was also observed that the yellow solutions containing both 4-NA and 4-NPD became colorless. All these findings suggest that the ACF-Pd catalyst successfully converted 4-NA to 1,4-phenylenediamine and 4-NPD to 1,2,4-benzenetriamine. Through kinetic studies, the rate constants for the catalytic reduction of nitroaromatics were calculated using the following Eq. (3). As a result of these calculations, the rate constants for the catalytic reductions of 2-NA, 4-NP,

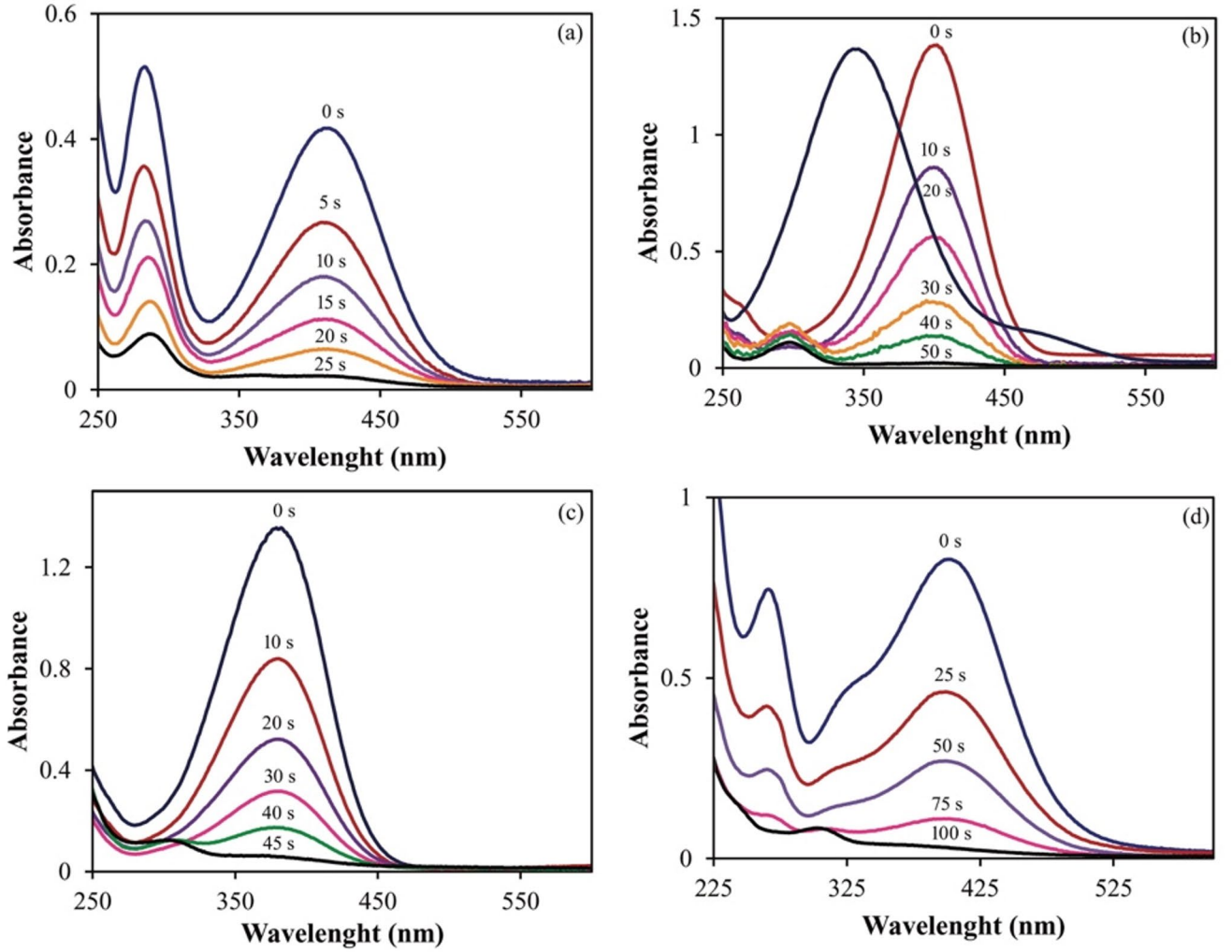


Fig. 9 UV-Vis spectra of the catalytic reductions of (**a**) 2-NA, (**b**) 4-NP, (**c**) 4-NA and (**d**) 4-NPD in the presence of AC-Pd

4-NA and 4-NPD catalyzed by the ACF-Pd catalyst were found to be $0.028s^{-1}$, $0.016s^{-1}$, $0.037s^{-1}$ and $0.011s^{-1}$, respectively (Fig. 10).

$$ln\frac{C_t}{C_o} = -kt \tag{3}$$

C_t and C_0 represent the concentrations of organic pollutants at the measured reaction time (t) and initial reaction time, respectively, while k (s^{-1}) denotes the rate constant.

Considering the successful performance of the ACF-Pd catalyst in the catalytic reduction of nitroaromatics, the efficiency of the catalyst in the catalytic reduction of different organic dyes, such as MO, MB and RhB, was also evaluated. It is known that activated carbons with pore size less than 2 nm (microporous structure) cannot be used for absorbent for reduction of large-sized molecules such as rhodamine B and methyl orange etc [64–66]. As revealed by BET analyses, ACF-Pd with its mesoporous structure can be used in reduction of organic pollutants. A proposed degradation mechanism for rhodamine B and methylene blue into their leuco–derivatives given in Fig. 11. First step hydride ions were transferred on Pd–NPs on microbeads from sodium borohydride and then rhodamine B and methylene blue were adsorbed on microbeads. The transferred electrons from hydride on Pd–NPs reduces the organic dye molecules to their low toxic leuco–derivatives. Finally, Pd–NPs desorption hydrogel beads rejoin to the cycle after desorption of the leuco–derivatives from surface of catalyst [67].

As seen in Fig. 12, the aqueous solution of MO showed strong absorbance band at 466 nm, the aqueous solution of RhB at 556 nm, and the aqueous solution of MB at 667 nm. The ACF-Pd catalyst was added separately to the mixtures of MO+$NaBH_4$, RhB+$NaBH_4$ and MB+$NaBH_4$ and the reactions were followed by recording UV-Vis spectra at different time intervals. Upon adding the ACF-Pd catalyst to

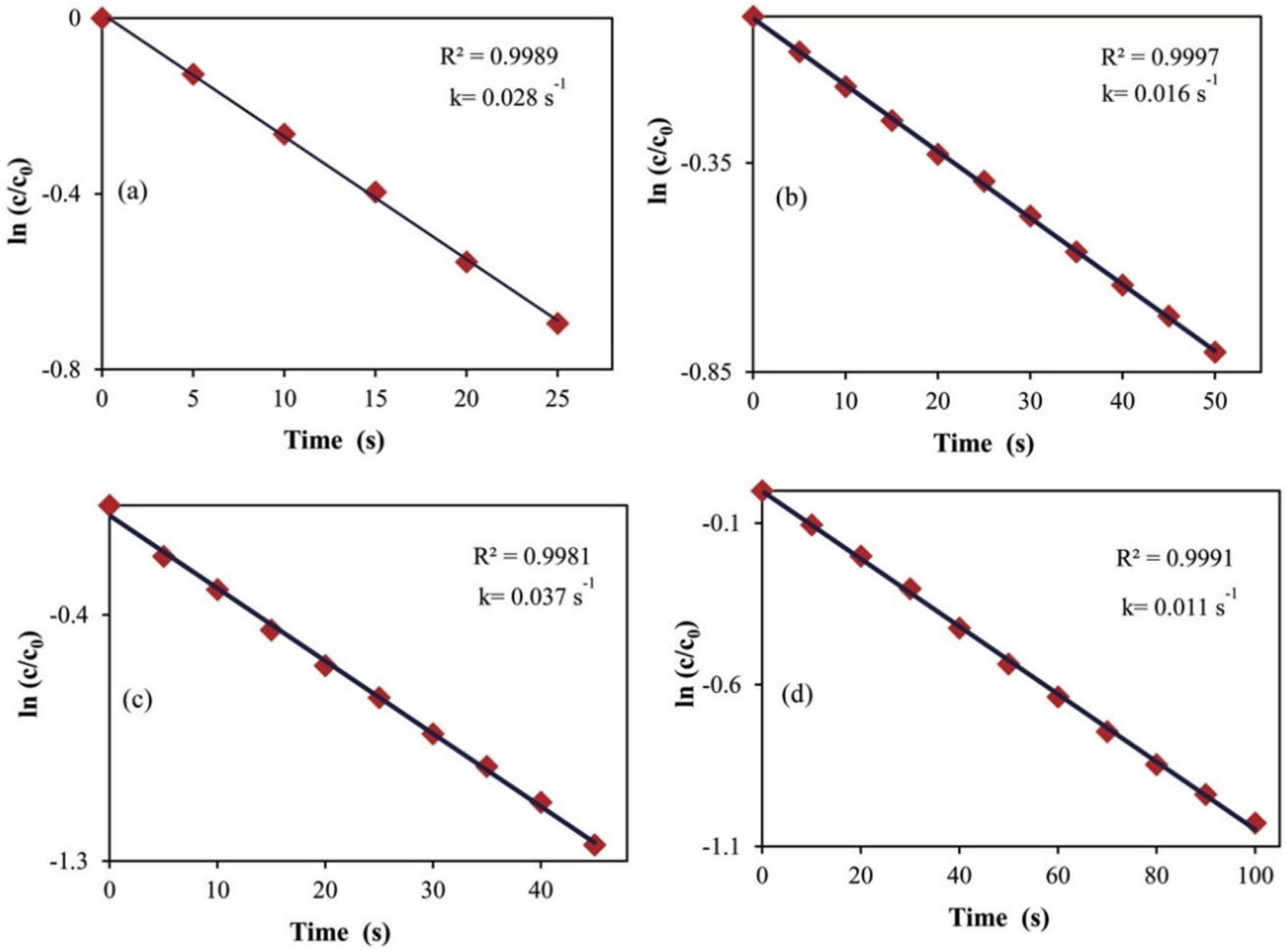


Fig. 10 Rate constants for the catalytic reductions of 2-NA (**a**), 4-NP (**b**), 4-NA (**c**), and 4-NPD (**d**) using ACF–Pd catalyst

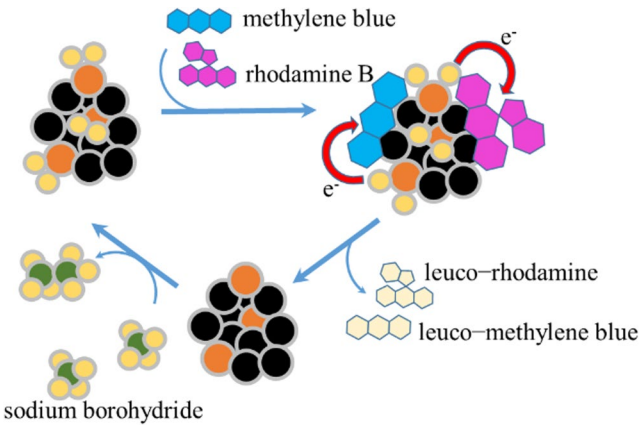


Fig. 11 Proposed reaction mechanism for catalytic conversion of methylene blue and rhodamine B to leuco–derivatives

the aqueous solution of MO+$NaBH_4$ and RhB+$NaBH_4$, the intensities of the characteristic absorbance bands of both MO and RhB decreased and completely disappeared in 20 s and 55 s, respectively. After the reduction of RhB and MO, it was observed that the solution turns colorless by the end of the reaction. These findings revealed that the ACF-Pd catalyst play an active role in both MO and RhB reductions. On the other hand, when the ACF-Pd catalyst was added to the mixture of MB and $NaBH_4$, the absorbance band of MB at 667 nm disappeared immediately, and the solution became colorless. This result confirms that ACF-Pd catalyst rapidly facilitated the catalytic reduction of MB. Also, in the presence of the ACF-Pd catalysts, the rate constants for the reduction of MO and RhB were found to be 0.034 s^{-1} and 0.031 s^{-1}, respectively, using the above equation (Fig. 13).

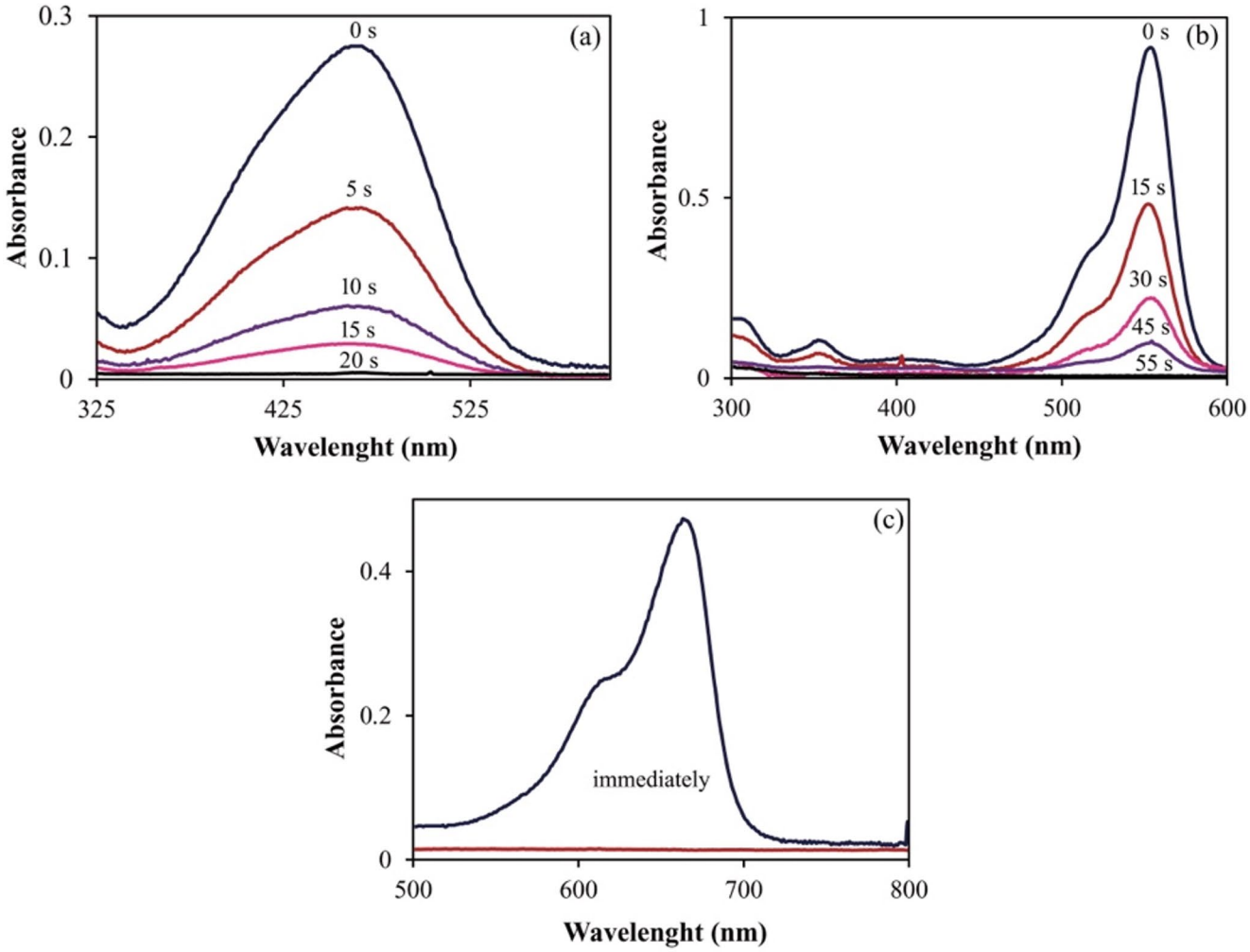


Fig. 12 UV-Vis spectra of the catalytic reductions of organic dyes (**a**) MO (**b**) RhB and (**c**) MB in the presence of AC-Pd

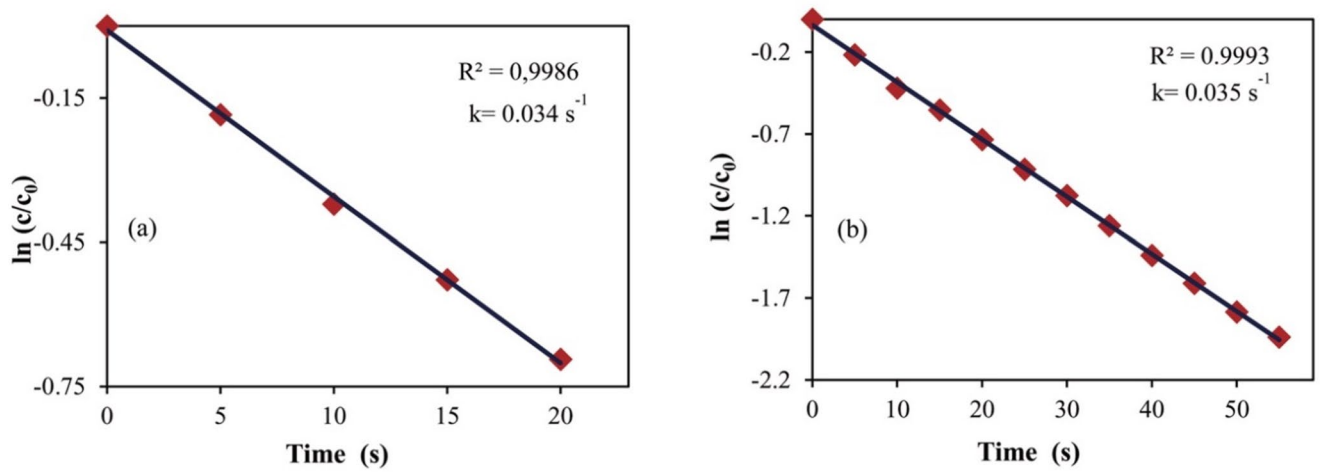


Fig. 13 Plots of ln (c_t/c_0) versus reaction time for catalytic reductions of (**a**) MO and (**b**) RhB dyes in the presence of AC-Pd

Table 3 The catalytic performance of ACF-Pd with different catalysts for the reduction of 4–NP, MO, RhB, and MB

Pollutant	Catalyst	Time	Rate constant (k)	Ref.
4–NP	GO-DAP-AgNPs	12 min	7.548×10^{-4} s^{-1}	[68]
	Au NPs@C longa.	100s	0.019 s^{-1}	[69]
	Fe_3O_4@ILD-CoCu	180s	0.366 min^{-1}	[70]
	nZVI-FBC	10 min	0.251 min^{-1}	[71]
	Ag/CA	10 min	0.34 min^{-1}	[72]
	PdNPs/NC	16 min	0.1144 min^{-1}	[73]
	Au/CB	5 min	0.8302 min^{-1}	[74]
	ACF-Pd	50 s	0.016 s^{-1}	Present study
MO	NWs-Pd80	10 min	0.4985 min^{-1}	[75]
	Cu-Ag/GP	4 min	7.67×10^{-3} s^{-1}	[76]
	Ag/TiO_2	9 min	-	[77]
	0.3Ag/HA	5 (±0.15) min	0.92 (±0.045) min^{-1}	[78]
	Pt/AC catalyst	80 s	3.08×10^{2} s^{-1}	[79]
	ACF-Pd	20 s	0.034 s^{-1}	Present study
RhB	S-2 catalyst	14 min	3.73×10^{-1} s^{-1}	[80]
	Ag NPs/Thymbra	50 s	8.64×10^{-2} s^{-1}	[81]
	CuNiOS-0.6	60 s	13×10^{-2} s^{-1}	[82]
	Cu/GO/MnO_2	4 min	-	[83]
	Pt-Cu nps	40 s	4.5×10^{-2} s^{-1}	[67]
	ACF-Pd	55 s	0.035 s^{-1}	Present study
MB	Fe_3O_4@TA/Ag	40s	0.0685 s^{-1}	[84]
	Ni/CPM-1	13 min	0.583 min^{-1}	[85]
	BCDs-Ag/MNPs	60s	0.0656 s^{-1}	[86]
	ACF-Pd		-	Present study

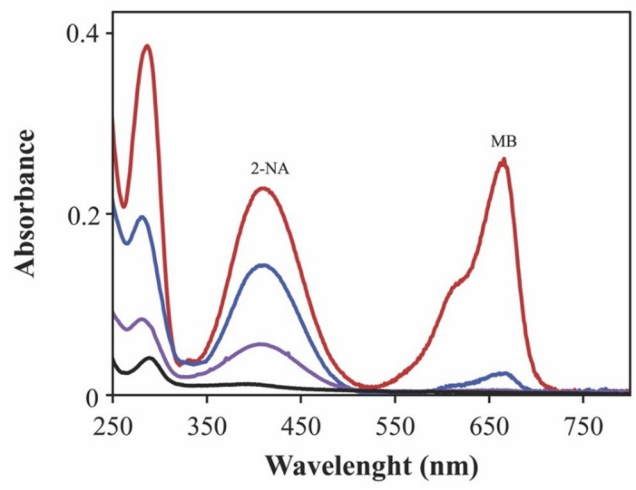


Fig. 14 UV-Vis spectrum of catalytic reduction of [2-NA+MB] mixture using ACF–Pd catalyst

Table 3 shows a comparison of the performance of ACF-Pd with other catalysts reported in the literature for the reduction of 4–NP, MO, RhB, and MB. The ACF-Pd catalyst in the present study demonstrated better performance compared to other catalysts, based on reaction time or rate constant.

On the other hand, to evaluate the broad applicability of the synthesized ACF–Pd catalyst, its performance was tested in the reduction of [2-NA+MB] mixture under the previously optimized reaction conditions, and the corresponding UV–Vis spectra are shown in Fig. 14. As can be seen in Fig. 14, the ACF–Pd catalyst successfully reduced MB within 5 s and 2-NA within 30 s. These results demonstrate that the ACF–Pd catalyst also exhibits excellent performance in the presence of mixed substrates.

The recovery and reusability of the synthesized ACF-Pd catalyst was investigated using the optimum reaction parameters determined for the catalytic reduction of 2-NA. After the first cycle, the ACF-Pd catalyst recovered from the reaction medium by filtration, reactivated by washing with water and ethanol, and dried for use in subsequent studies. This process was repeated at the end of each cycle. The reusability tests showed that the ACF-Pd catalyst successfully performed the catalytic reduction of 2-NA for 5 consecutive reactions, almost without losing its activity. Additionally, EDS analysis of the used ACF–Pd catalyst was carried out for comparison with the fresh ACF–Pd catalyst, and the corresponding spectrum is shown in Fig. 15. The distinct presence of Pd peaks in the spectrum clearly confirms that the ACF–Pd catalyst preserves its stability and durability after reuse.

4 Conclusion

In conclusion, the catalytic reduction property and kinetic rate constants of the ACF-Pd catalyst were determined using four different nitroaromatics (2-NA, 4-NP, 4-NA and 4-NPD) and three different organic dyes (MO, MB and RhB). The reduction reactions followed a decrease in the characteristic absorbance peaks of both nitroaromatics and organic dyes over the reaction times.

Accordingly, catalytic degradation of 2-NA and its rate constant were calculated as 0.028 s^{-1}, respectively, and 2-NA converted to o-phenylenediamine; 4-NP showed within 50 s and 0.016 s^{-1}, and the reaction occurred via 4-nitrophenolate and 4-aminophenol was formed; 4-NA was observed in 45 s and 0.037 s^{-1} and converted to 1,4-phenylenediamine; 4-NPD was observed in 100 s and 0.011 s^{-1} and converted to 1,2,4-benzenetriamine. The catalytic degradation and rate constant for organic dyes of MO and RhB were observed within 20 s and 0.034 s^{-1}, and 55 s and 0.031 s^{-1}, respectively, while MB degraded immediately. The ACF-Pd catalyst in this study showed better performance compared to other catalysts

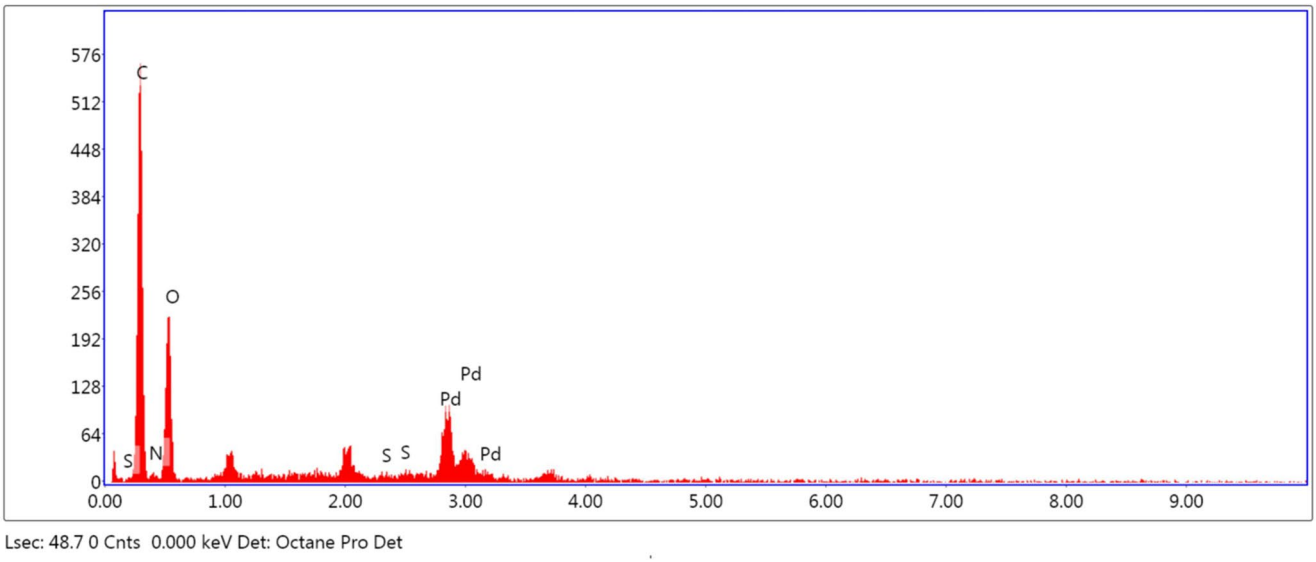


Fig. 15 EDS spectrum of used ACF–Pd catalyst

depending on the reaction time or rate constant. The recovery and reusability of the synthesized ACF-Pd catalyst was tested and showed that 2-NA showed the best performance and successfully carried out its catalytic reduction over five consecutive reactions almost without losing its activity.

Acknowledgements This study was supported by Recep Tayyip Erdogan University—Research Funding—(FBA-2023-1418).

Author contributions Z.Ö and H.T.A studied activated carbon and its of characterization. K.K prepared and studied Figs. 5 and 6. T.B and N.Y.B studied catalytic degradation. All authors reviewed the manuscript.

Funding Open access funding provided by the Scientific and Technological Research Council of Türkiye (TÜBİTAK).

Data availability No datasets were generated or analysed during the current study.

Declarations

Ethics and Consent to Participate not applicable.

Competing interests The authors declare no competing interests.

Conflicts of interests The authors have no conflicts of interest to declare that are relevant to the content of this article.

Open Access This article is licensed under a Creative Commons Attribution 4.0 International License, which permits use, sharing, adaptation, distribution and reproduction in any medium or format, as long as you give appropriate credit to the original author(s) and the source, provide a link to the Creative Commons licence, and indicate if changes were made. The images or other third party material in this article are included in the article's Creative Commons licence, unless indicated otherwise in a credit line to the material. If material is not included in the article's Creative Commons licence and your intended use is not permitted by statutory regulation or exceeds the permitted use, you will need to obtain permission directly from the copyright holder. To view a copy of this licence, visit http://creativecommons.org/licenses/by/4.0/.

References

1. M. Ariannezhad, N. Pourmorteza, A. Yousefi, M. Esperi, Chem. Phys. Lett. **793**, 139431 (2022)
2. S. Doherty, J.G. Knight, T. Backhouse, A. Bradford, F. Saunders, R.A. Bourne, T.W. Chamberlain, R. Stones, A. Clayton, K. Lovelock, Catal. Sci. Technol. **8**, 1454 (2018)
3. K. Karaoğlu, Z. Özçifçi, M. Çalışkan, T. Baran, H.T. Akçay, Mater. Chem. Phys. **282**, 125857 (2022)
4. F. Rafiee, M. Rezaee, React. Funct. Polym. **172**, 105208 (2022)
5. R.M. Lunn, S.S. Mehta, G.D. Jahnke, A. Wang, M.S. Wolfe, B.R. Berridge, JNCI: J. Natl. Cancer Inst. **114**, 1441 (2022)
6. J. Tiwari, P. Tarale, S. Sivanesan, A. Bafana, Environ. Sci. Pollut. Res. **26**, 28650 (2019)
7. M. Bilal, A.R. Bagheri, P. Bhatt, S. Chen, J. Environ. Manage. **291**, 112685 (2021)
8. J.C. Maxwell, B.C. Baker, C.F.J. Faul, ACS Appl. Polym. Mater. **5**, 662 (2023)
9. M. Farhan Hanafi, N. Sapawe, Mater. Today Proc. **31**, A141 (2020)
10. M. Ismail, K. Akhtar, M.I. Khan, T. Kamal, M.A. Khan, A.M. Asiri, J. Seo, S.B. Khan, Curr. Pharm. Des. **25**, 3645 (2019)
11. X. Chun Song, Z. Ai Yang, Y. Fan, Zheng, and H. Yong Yin, Curr Nanosci 9, 128 (2013)
12. S. Venkatesan, S. Suresh, P. Ramu, J. Arumugam, S. Thambidurai, N. Pugazhenthiran, Results Chem. **4**, 100637 (2022)
13. D. Chen, Y. Cheng, N. Zhou, P. Chen, Y. Wang, K. Li, S. Huo, P. Cheng, P. Peng, R. Zhang, L. Wang, H. Liu, Y. Liu, R. Ruan, J. Clean. Prod. **268**, 121725 (2020)
14. K. Karaoğlu, H.T. Akçay, Z. Özçifçi, M. Çalışkan, T. Baran, Ceram. Int. **47**, 27816 (2021)
15. H.T. Akçay, A. Demir, Z. Özçifçi, T. Yumak, T. Keleş, Carbon Lett. **33**, 1445 (2023)
16. K. Karaoğlu, G.D. Yüzüak, E. Yüzüak, H. Turan, H.T. Akçay, Mater. Sci. Semicond. Process. **177**, 108392 (2024)
17. N.Y. Baran, M. Çalışkan, A. Özpala, T. Baran, Int. J. Biol. Macromol. **265**, 131130 (2024)

18. M.H. Abdel-Khalek, M.A. Ahmed, M.F. Abdel-Messih, F. El-Shahat, Mater. Sci. Energy Technol. **5**, 334 (2022)
19. Y. Yin, M. Liu, L. Shi, S. Zhang, R.A.K. Hirani, C. Zhu, C. Chen, A. Yuan, X. Duan, S. Wang, H. Sun, J. Hazard. Mater. **435**, 128939 (2022)
20. H.S. Bae, R.P. Patil, J.H. Hwang, M.A. Mahadik, M.S. Song, W.S. Chae, V. Manikandan, J.S. Jang, J. Environ. Chem. Eng. **11**, 109837 (2023)
21. K. Karaoğlu, Z. Özçifçi, M. Çalışkan, H. Türker, Akçay, T. Baran, Inorg. Chem. Commun. **154**, 110950 (2023)
22. P. Xie, W. Zhang, W. Wu, Z. Shen, M. Wang, Y. Lai, Y. Chen, Z. Jia, Int. J. Biol. Macromol. **215**, 606 (2022)
23. A.H. Alneyadi, S.S. Ashraf, Chem. Eng. J. **303**, 529 (2016)
24. H. Wang, L.X. Tang, Y.F. Ye, J.X. Ma, X. Li, J. Si, B.K. Cui, J. Environ. Manage. **359**, 120984 (2024)
25. H. Lin, K. Xu, W. Chen, C. Fang, P. Liu, Colloid Interface Sci. Commun. **58**, 100765 (2024)
26. R. Wazalwar, M. Sahu, A.M. Raichur, Nanoscale Adv. **3**, 2741 (2021)
27. J. Im, Y.H. Jeong, M.C. Kim, D. Oh, J. Son, K. Hyun, B. Jeong, S. Hong, J. Lee, Carbon N Y. **216**, 118532 (2024)
28. A.H. Alateah, Case Stud. Constr. Mater. **19**, e02653 (2023)
29. H. Dai, Acc. Chem. Res. **35**, 1035 (2002)
30. M.J.G. De Araújo, J. Villarroel-Rocha, V.C. De Souza, K. Sapag, S.B.C. Pergher, J. Anal. Appl. Pyrol. **141**, 104627 (2019)
31. Z. Özçifçi, M. Emirik, H.T. Akçay, T. Yumak, Colloids Surf. Physicochem Eng. Asp. **690**, 133851 (2024)
32. Z. Özçifçi, M.A. Özşanlı, H.T. Akçay, T. Yumak, J. Porous Mater. **30**, 797 (2023)
33. G.A. Gebreslase, D. Sebastián, M.V. Martínez-Huerta, T. Tsoncheva, B. Tsyntsarski, G. Georgiev, M.J. Lázaro, Catal. Today. **423**, 113991 (2023)
34. Y. Chen, L. Jiang, S. Lin, P. Dong, X. Fu, Y. Wang, Q. Liu, M. Wu, Molecules. **29**, 4628 (2024)
35. P. Summa, M. Motak, P. Da, Costa, Catalysts. **14**, 11 (2023)
36. M.R. Benzigar, S.N. Talapaneni, S. Joseph, K. Ramadass, G. Singh, J. Scaranto, U. Ravon, K. Al-Bahily, A. Vinu, Chem. Soc. Rev. **47**, 2680 (2018)
37. Á. Prekob, Á. Szamosvölgyi, G. Muránszky, J. Lakatos, Z. Kónya, B. Fiser, B. Viskolcz, L. Vanyorek, Int. J. Mol. Sci. **23**, 6423 (2022)
38. L.F. Velasco, B. Tsyntsarski, B. Petrova, T. Budinova, N. Petrov, J.B. Parra, C.O. Ania, J. Hazard. Mater. **184**, 843 (2010)
39. R. Rimi, Kumar, B. Uttam, Chempluschem **89**, (2024)
40. Y. Li, Y. Guo, Z. Jing, X. Zhao, Y. Zhou, M. Shuai, Mater. Today Commun. **34**, 105089 (2023)
41. M. Orlandi, D. Brenna, R. Harms, S. Jost, M. Benaglia, Org. Process. Res. Dev. **22**, 430 (2018)
42. S. Taheri, M.M. Heravi, A. Saljooqi, Sci. Rep. **13**, 17566 (2023)
43. J. Liu, X. Yan, L. Wang, L. Kong, P. Jian, J. Colloid Interface Sci. **497**, 102 (2017)
44. S. Brunauer, P.H. Emmett, E. Teller, J. Am. Chem. Soc. **60**, 309 (1938)
45. A.V. Neimark, Y. Lin, P.I. Ravikovitch, M. Thommes, Carbon N Y. **47**, 1617 (2009)
46. G. HORVÁTH, K. KAWAZOE, JOURNAL OF CHEMICAL, Eng. JAPAN. **16**, 470 (1983)
47. M.S. Bafghi, M. Karimi, M. Adeli, Iran. J. Mater. Sci. Eng. **10**, 18 (2013)
48. Q. Chen, X. Liu, T. Wang, X. Su, M. Liu, S. Chaemchuen, F. Verpoort, J. Mater. Sci. Technol. **149**, 255 (2023)
49. A.E. Ogungbenro, D.V. Quang, K.A. Al-Ali, L.F. Vega, M.R.M. Abu-Zahra, J. Environ. Chem. Eng. **8**, 104257 (2020)
50. M. Armandi, B. Bonelli, F. Geobaldo, E. Garrone, Microporous Mesoporous Mater. **132**, 414 (2010)
51. G.P.S. Maciel, E. Lazzari, T. Bjerk, S.M. Ahmad, A.P. Carvalho, J.M.F. Nogueira, E.B. Caramão, Int. J. Eng. Res. Sci. **3**, 46 (2017)
52. M. Thommes, K. Kaneko, A.V. Neimark, J.P. Olivier, F. Rodriguez-Reinoso, J. Rouquerol, K.S.W. Sing, Pure Appl. Chem. **87**, 1051 (2015)
53. S.H. Pak, M.J. Jeon, Y.W. Jeon, Int. Biodeterior. Biodegradation. **113**, 195 (2016)
54. A.C. Ferrari, J. Robertson, Phys. Rev. B **61**, 14095 (2000)
55. F. Tuinstra, J.L. Koenig, J. Chem. Phys. **53**, 1126 (1970)
56. J. Chantaramethakul, C. Hussakan, Y. Yenmankhong, P. Chandeang, R. Techapiesancharoenkij, W. Hirunpinyopas, C. Kasmui, Kurniawan, G. Panomsuwan, RSC Adv. **14**, 31648 (2024)
57. A. Taylor, J. Chem. Technol. Biotechnol. **53**, 215 (1992)
58. F. Vautard, S. Ozcan, F. Paulauskas, J.E. Spruiell, H. Meyer, M.J. Lance, Appl. Surf. Sci. **261**, 473 (2012)
59. A.M. Puziy, O.I. Poddubnaya, R.P. Socha, J. Gurgul, M. Wisniewski, Carbon N Y. **46**, 2113 (2008)
60. I. Velo-Gala, J.J. López-Peñalver, M. Sánchez-Polo, J. Rivera-Utrilla, Carbon N Y. **67**, 236 (2014)
61. X.-Y. Liu, M. Huang, H.-L. Ma, Z.-Q. Zhang, J.-M. Gao, Y.-L. Zhu, X.-J. Han, X.-Y. Guo, Molecules. **15**, 7188 (2010)
62. X. Wu, N.C. Gallego, C.I. Contescu, H. Tekinalp, V.V. Bhat, F.S. Baker, M.C. Thies, Carbon N Y. **46**, 54 (2008)
63. A.L. Patterson, Phys. Rev. **56**, 978 (1939)
64. J. Lee, S. Han, T. Hyeon, J. Mater. Chem. **14**, 478 (2004)
65. T.A. Saleh, A.A. Al-Saadi, Surf. Interface Anal. **47**, 785 (2015)
66. T. Kyotani, Carbon N Y. **38**, 269 (2000)
67. H.P. Singh, N. Gupta, S.K. Sharma, R.K. Sharma, Colloids Surf. Physicochem Eng. Asp. **416**, 43 (2013)
68. J. Nimita Jebaranjitham, C. Mageshwari, R. Saravanan, N. Mu, Compos. B Eng. **171**, 302 (2019)
69. W. Xie, Y. Zhang, X. Yang, P. Yu, D. Ban, Inorg. Chem. Commun. **162**, 112169 (2024)
70. M. Gholinejad, M. Ali Saidiansar, M. Eskandari, J.M. Sansano, Polyhedron. **259**, 117059 (2024)
71. A. Bashir, A.H. Pandith, A. Qureashi, L.A. Malik, M. Gani, J.M. Perez, J. Environ. Chem. Eng. **10**, 107401 (2022)
72. T. Gia-Thien Ho, B.L. Do, B. Van Pham, T.T. Van Nguyen, H.P. Phan, H.B. Nguyen, P.P.T. Vo, N. Tri, RSC Adv. **12**, 25753 (2022)
73. T. Dang-Bao, L.N. Nguyen, H.H. Lam, Mater. Today Proc. (2023)
74. L. Qin, H. Yi, G. Zeng, C. Lai, D. Huang, P. Xu, Y. Fu, J. He, B. Li, C. Zhang, M. Cheng, H. Wang, X. Liu, J. Hazard. Mater. **380**, 120864 (2019)
75. J. Ashraf, G.A. Khan, M. ul Ain, M.A. Ghanem, K.M.H. Mohammed, W. Ahmed, Inorg. Chem. Commun. **169**, 113039 (2024)
76. M. Ismail, M.I. Khan, S.B. Khan, M.A. Khan, K. Akhtar, A.M. Asiri, J. Mol. Liq. **260**, 78 (2018)
77. M. Atarod, M. Nasrollahzadeh, S. Mohammad Sajadi, J. Colloid Interface Sci. **462**, 272 (2016)
78. B.K. Ghosh, S. Hazra, B. Naik, N.N. Ghosh, Powder Technol. **269**, 371 (2015)
79. S.A.A. Vandarkuzhali, S. Karthikeyan, B. Viswanathan, M.P. Pachamuthu, Surf. Interfaces. **13**, 101 (2018)
80. X. Yang, H. Zhong, Y. Zhu, H. Jiang, J. Shen, J. Huang, C. Li, J. Mater. Chem. Mater. **2**, 9040 (2014)
81. H. Veisi, S. Azizi, P. Mohammadi, J. Clean. Prod. **170**, 1536 (2018)
82. A.K. Abay, X. Chen, D.-H. Kuo, New J. Chem. **41**, 5628 (2017)
83. S. Naghdi, M. Sajjadi, M. Nasrollahzadeh, K.Y. Rhee, S.M. Sajadi, B. Jaleh, J. Taiwan. Inst. Chem. Eng. **86**, 158 (2018)
84. H. Veisi, S.B. Moradi, A. Saljooqi, P. Safarimehr, Mater. Sci. Engineering: C **100**, 445 (2019)
85. P. Veerakumar, S.-M. Chen, R. Madhu, V. Veeramani, C.-T. Hung, S.-B. Liu, ACS Appl. Mater. Interfaces. **7**, 24810 (2015)
86. M. Zahedifar, N. Seyedi, M. Salajeghe, S. Shafiei, Mater. Chem. Phys. **246**, 122789 (2020)

Publisher's note Springer Nature remains neutral with regard to jurisdictional claims in published maps and institutional affiliations.